

GeoTexDensifier: Geometry-Texture-Aware Densification for High-Quality Photorealistic 3D Gaussian Splatting

Hanqing Jiang, Xiaojun Xiang, Han Sun, Hongjie Li, Liyang Zhou, Xiaoyu Zhang,
Guofeng Zhang, *Member, IEEE*

Abstract—3D Gaussian Splatting (3DGS) has recently attracted wide attentions in various areas such as 3D navigation, Virtual Reality (VR) and 3D simulation, due to its photorealistic and efficient rendering performance. High-quality reconstruction of 3DGS relies on sufficient splats and a reasonable distribution of these splats to fit real geometric surface and texture details, which turns out to be a challenging problem. We present GeoTexDensifier, a novel geometry-texture-aware densification strategy to reconstruct high-quality Gaussian splats which better comply with the geometric structure and texture richness of the scene. Specifically, our GeoTexDensifier framework carries out an auxiliary texture-aware densification method to produce a denser distribution of splats in fully textured areas, while keeping sparsity in low-texture regions to maintain the quality of Gaussian point cloud. Meanwhile, a geometry-aware splitting strategy takes depth and normal priors to guide the splitting sampling and filter out the noisy splats whose initial positions are far from the actual geometric surfaces they aim to fit, under a *Validation of Depth Ratio Change* checking. With the help of relative monocular depth prior, such geometry-aware validation can effectively reduce the influence of scattered Gaussians to the final rendering quality, especially in regions with weak textures or without sufficient training views. The texture-aware densification and geometry-aware splitting strategies are fully combined to obtain a set of high-quality Gaussian splats. We experiment our GeoTexDensifier framework on various datasets and compare our Novel View Synthesis results to other state-of-the-art 3DGS approaches, with detailed quantitative and qualitative evaluations to demonstrate the effectiveness of our method in producing more photorealistic 3DGS models.

Index Terms—3D Gaussian Splatting, adaptive density control, texture-aware densification, geometry-aware splitting.

I. INTRODUCTION

RECENT years, 3D Gaussian Splatting (3DGS) [1] has attracted widespread attentions due to its efficient rendering performance and photorealistic visualization effects, and shown potential usefulness in various areas such as 3D navigation, Virtual Reality (VR), Mixed Reality (MR), 3D simulation and digital twins. Compared to the traditional Multi-View

Hanqing Jiang, Xiaojun Xiang, Han Sun, Hongjie Li, Liyang Zhou and Xiaoyu Zhang are with SenseTime Research. E-mails: {jianghanqing, xiangxiaojun, sunhan, lihongjie2, zhoulilyang, zhangxiaoyu}@sensetime.com.

Guofeng Zhang is with the State Key Lab of CAD&CG, Zhejiang University. E-mail: zhangguofeng@zju.edu.cn.

Corresponding Author: Guofeng Zhang.

Hanqing Jiang, Xiaojun Xiang and Han Sun assert equal contribution and joint first authorship.

Stereo (MVS) [2], [3] and texture mapping [4] methods which reconstruct explicit mesh models, 3DGS models are able to present more realistic texture and appearance details in online performance. Additionally, compared to the implicit representation of Neural Radiance Fields (NeRF) like [5], [6], [6], [7], 3DGS innovatively proposes to use a set of differentiable 3D Gaussian ellipsoids called splats to represent the explicit structure of the captured scene, which more friendly support graphics techniques like editing [8]–[11], relighting [12] and physical simulation [13] of the Gaussian splats in 3D space.

3DGS achieves complete scene reconstruction and texture detail enhancement through the splitting and cloning of initial Gaussian points. High-quality reconstruction and rendering of 3DGS models rely on two conditions: the first is to have a sufficient number of Gaussian splats to support appearance details, and the second is to ensure that the splats are optimized to the correct positions in 3D space. Currently, very few studies have explored the improvement of Gaussian splat densification strategy. For instance, Mini-Splatting [14] introduces blur split strategy to further densify Gaussians with very large scales, but might generate a denser and more uniform spatial distribution with too many Gaussians, which is alleviated by additional simplification. An optimal but challenging densification strategy is to further densify splat distribution in fully textured areas, and still leave Gaussians sparse in more weakly textured regions. There are even fewer works discussing the geometrically accurate positioning of Gaussian splats. GeoGaussian [15] transfers thin splats aligned with the smoothly connected areas observed from point cloud to newly generated ones through a carefully designed densification strategy, but relies heavily on the surfaces detected from the recovered splats in textureless regions which are usually noisy. Actually, for textured areas, there are usually sufficient multi-view visual cues for optimizing the Gaussian points to the accurate positions or remove the incorrect ones during the training process, while in textureless regions however, the lack of adequate visual observations makes it challenging to ensure the correct positioning of Gaussian splats.

To better tackle both densification and positioning problems mentioned above, this paper presents a novel 3D Gaussian splatting framework for high-quality photorealistic novel view rendering, which we named GeoTexDensifier. Our framework innovatively proposes a densification strategy that enforces the

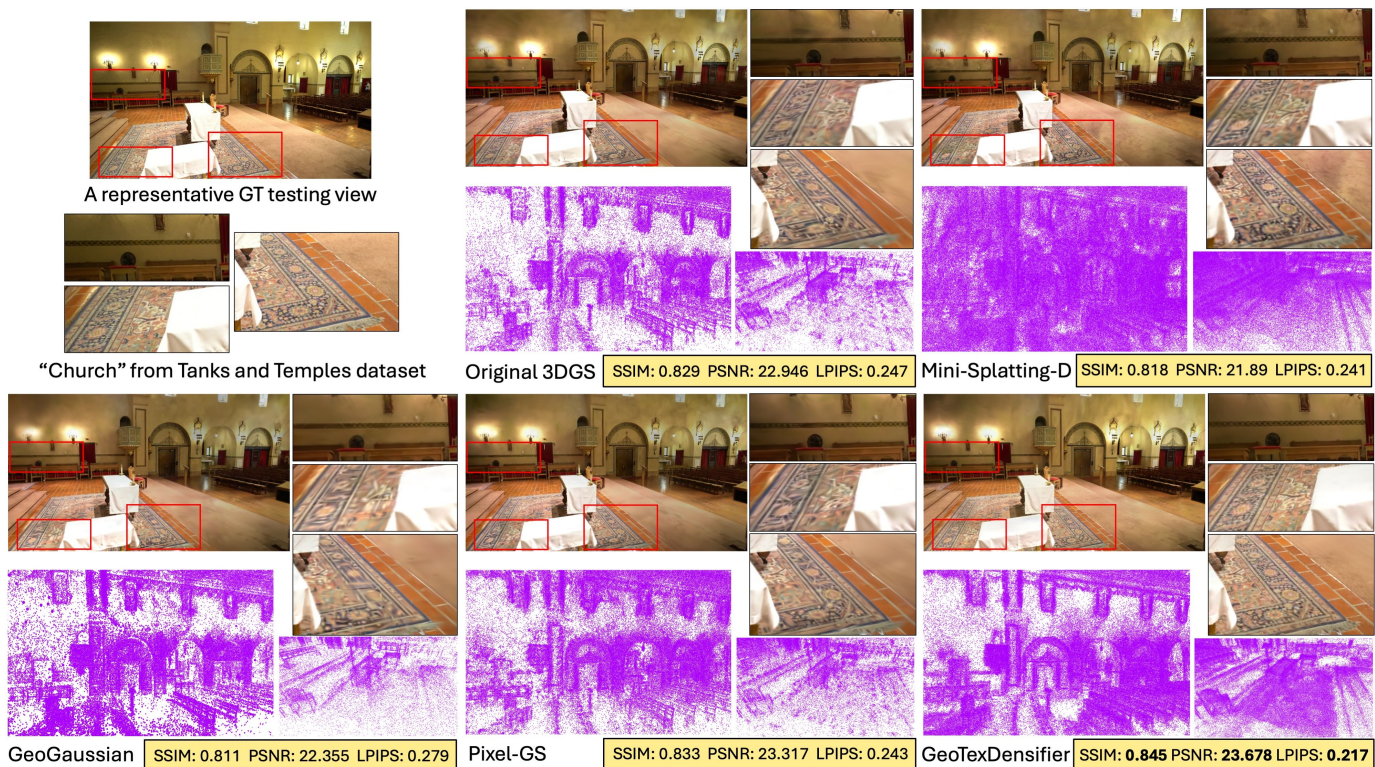


Fig. 1. 3DGS reconstruction of the case “Church” from Tanks and Temples dataset [16]. A representative source image is taken as GT testing view. The reconstructed 3D Gaussian point clouds by original 3DGS [1], Mini-Splatting-D [14], GeoGaussian [15], Pixel-GS [17] and our GeoTexDensifier are given together with their respective rendered images in the testing views, to show that our framework performs the best in both spatial distribution of Gaussian splats and photorealistic rendering results, as verified by the rendering quality evaluation on SSIM, PSNR in dB, and LPIPS.

reconstructed Gaussians to more accurately comply with the actual geometric structure of the scene. Moreover, our densified Gaussian model contains a sufficient number of splats to support fully textured regions, while maintaining sparse Gaussian splat distribution in weakly textured areas. In these ways, our novel 3DGS framework is able to produce high-quality 3D Gaussian models, as shown in the comparative example of “Church” in Fig. 1. The original 3DGS [1] has “over-reconstruction” problem that causes missing details in textured regions such as the carpet, while state-of-the-art (SOTA) works like GeoGaussian [15] improves the spatial structure of splat distribution and Pixel-GS [17] further densifies the splats in some textured regions like the carpet, but both of them still lack sufficient splat sampling to support texture details. Mini-Splatting [14] has sufficiently sampled splats but introduces over-densification situation in textureless regions, which might produce extra noisy Gaussians due to underconstrained visual ambiguity. In comparison, our GexTexDensifier delivers more accurate spatial distribution of Gaussian splat with less noise and more photorealistic novel view rendering effects according to the quantitative evaluation of the rendering results in the ground truth (GT) testing views on metrics of Structural SIMilarity (SSIM), Peak Signal to Noise Ratio (PSNR) in dB, and Learned Perceptual Image Patch Similarity (LPIPS). Our GeoTexDensifier framework carries out a geometry-aware splitting strategy to guide the splitting position sampling to fit the actual geometric surfaces of the scene with the help of normal prior, and filter out noisy splats with improper initial

positions according to our *Validation of Depth Ratio Change* checking on relative depths provided by monocular depth prior. Meanwhile, a texture-aware densification strategy is adopted as auxiliary supplement for splitting of additional large Gaussians to produce a denser splat distribution in highly textured regions while remaining sparse in weakly textured areas, thereby preserving the overall high quality of Gaussian point cloud. The texture-aware densification and geometry-aware splitting strategies are fully integrated in the iterative optimization to get the final high-quality photorealistic 3DGS model. Experiments on Mip-NeRF 360 [6], Tanks and Temples [16] datasets and self-captured scenes verify the effectiveness and robustness of our GeoTexDensifier pipeline.

In summary, our GeoTexDensifier framework contributes in the following main aspects:

- We innovatively propose a geometry-aware splitting strategy that takes normal and relative depth priors to more reasonably guide the position sampling of the split Gaussians and eliminate the improperly sampled splats whose positions are far from the real surfaces, to ensure well distributed splats which comply with the actual geometric structure of the scene.
- A texture-aware densification strategy is adopted as an auxiliary service for finding more contributive large splats in fully textured areas to be further split to fit texture details while keeping Gaussians sparse in weakly textured regions to maintain a high-quality spatial distribution of the recovered splats.

- Our GeoTexDensifier framework iteratively optimizes the distribution and parameters of Gaussians under the combination action of texture-aware densification and geometry-aware splitting to get photorealistic final 3DGS models with the best quality compared to SOTA works.

This paper is organized as follows. Section II presents works related to our approach. Section III gives an overview of the proposed GeoTexDensifier framework. Section IV briefly reviews the strategies of original 3DGS [1] and Mini-Splatting [14]. The texture-aware densification, geometry-aware splitting modules are described in sections V and VI respectively. Finally, we evaluate our GeoTexDensifier pipeline in section VII.

II. RELATED WORK

A. Novel View Synthesis

This paper studies Novel View Synthesis (NVS) field, which aims to generate realistic images of objects or scenes from unobserved viewpoints. NeRF [5] has become a standard work in this field, modeling 3D scenes as continuous functions of density and color using a large Multi-Layer Perceptron (MLP) network, which enables view generation through volume rendering but at a high computational cost for both training and rendering. Various advancements [6], [7], [18]–[23] aims at improving NVS quality and efficiency for training and perception. For example, Instant-NGP [19] proposed a multi-resolution hash encoding for automatic detail focusing and reduced computational cost. Mip-NeRF [18] replaced the point sampling mode with conical frustums and integrated positional encoding to address resolution-induced aliasing. The subsequent works Mip-NeRF 360 [6] and Zip-NeRF [7] were designed to handle unbounded scenes and to be compatible with grid-based representations, respectively. However, the costly MLP perception and implicit volumetric representation remain significant challenges for NeRF model to be time and memory efficiently navigated or edited for practical applications.

Recently, 3DGS [1] introduced a new approach for NVS, by utilizing splatting-based rasterization to project anisotropic 3D Gaussians onto 2D screen, and calculating pixel colors through depth sorting and α -blending. This splatting approach avoids complex ray marching to effectively enable real-time rendering for large-scale scenes, based on which several variants have emerged to further improve reconstruction scale [24], [25] and enhance photorealism [12], [26]–[28]. For example, both VastGaussian [24] and CityGaussian [25] address reconstruction and rendering of large-scale scenes, with the latter further optimizing the training approach and Level-of-Detail (LOD) strategy for more efficient rendering. Relightable 3D Gaussian [12] additionally introduces normals, BRDF parameters, and direction-dependent incident lighting for photorealistic relighting. During the Gaussian optimization process, Adaptive Density Control (ADC) plays a crucial role by determining where to expand or shrink the spatial distribution of Gaussian points, particularly in “under-reconstruction” and “over-reconstruction” regions. However, due to possibly noisy initialization and insufficient geometric constraints, the

growth of Gaussian splats can be undesirable particularly in textureless regions, leading to blur and artifacts in the rendered images. Some recent works have focused on this challenging problem, by proposing more reasonable densification strategies or introducing geometric priors for better ADC guidance to achieve better rendering results, which are discussed in detail in the following subsections.

B. Gaussian Densification Strategy

In the original 3DGS work [1], the growth of Gaussians is determined by the magnitude of the average positional gradient. However, large Gaussian splats in over-reconstructed regions often provide limited gradient values to support their splitting. To increase the likelihood of splitting in these regions, some approaches have modified the densification criteria. Bulò et al. [29] designed a auxiliary per-pixel error function as densification criteria, rather than relying solely on positional gradients. Pixel-GS [17] accounts for the maximal number of pixels each Gaussian contributes to different views as a compensational criteria to dynamically encourage splitting of large Gaussians. FreGS [30] employs progressive frequency regularization to increase the average pixel gradient for coarse-to-fine Gaussian densification. Some other approaches attempt to reorganize the scene structure to improve densification. For example, FSGS [31] organizes the scene into a graph structure based on proximity scores and defines new Gaussians at the edge centers, thereby enhancing control over ADC. Scaffold-GS [32] searches anchors to establish a hierarchical and region-aware scene representation for constraining the spatial splat distribution to avoid free drifting and splitting of Gaussians. GeoGaussian [15] detects smoothly connected areas from input point cloud and initializes each point as a thin ellipsoid aligned with smooth surfaces to enhance densification. Mini-Splatting [14] introduces blur split and depth reinitialization as densification strategies for facilitating a uniform spatial distribution of splats. These improved densification criterion commonly serve much like a compensational strategy to enrich the splats generated by the original work, while our GeoTexDensifier framework is an innovative strategy to make full use of geometry priors and texture gradients to guide our densification to a more accurate splat distribution.

C. Gaussian Optimization with Geometry Prior

Original 3DGS expects Gaussian splats expected to grow along the real scene surfaces, which is however not always conformed to. Consequently, some approaches have attempted to optimize Gaussians by incorporating geometric priors like depths and normals. Similar to MonoSDF [33], DN-Splatter [34] employs mono-depth and mono-normal estimates to constrain the rendering loss. DNGaussian [35] introduces Hard and Soft Depth Regularization to optimize the positions and opacities of Gaussians, and employs Global-Local Depth Normalization to mitigate the sensitivity of scale-invariant loss to small depth errors. PGSR [36] optimizes Gaussians by rendering unbiased depths combined with single-view and multi-view geometric consistency losses. Besides applying depth and normal constraints, both GaussianRoom [37] and

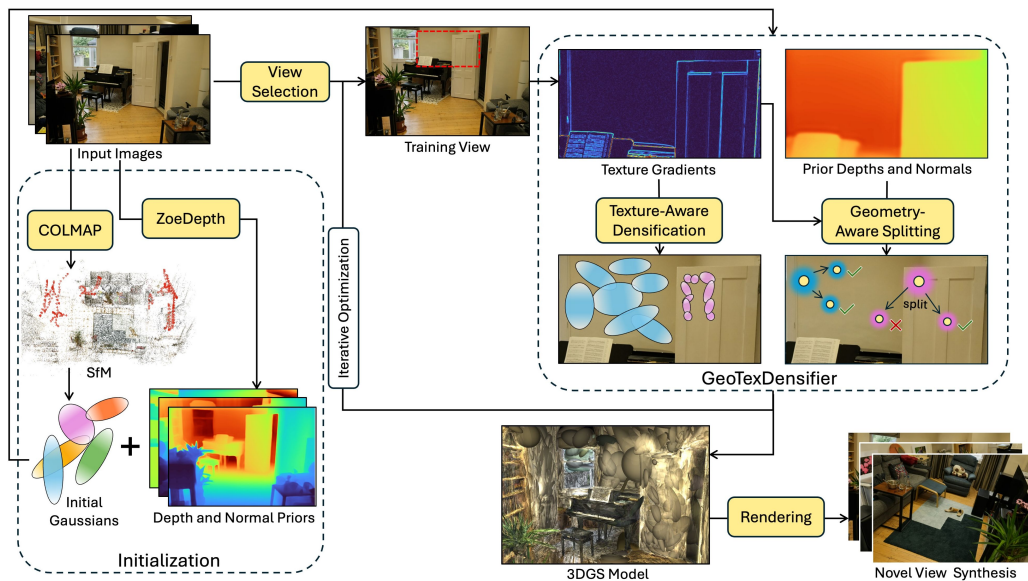


Fig. 2. System overview of our GeoTexDensifier, which consists of a geometry-aware splitting strategy for guiding the positioning of newly generated splats by depth and normal priors, and a texture-aware densification module which finds more contributive splats in fully textured areas to be further split to refine texture details in iterative optimization to get a well-structured 3DGS model with photorealistic rendering results.

GSDF [38] utilize a learnable neural SDF field to guide the growth of splats, so as to simultaneously optimize both SDF and Gaussians. These geometry prior based methods rely on the geometric accuracy of the prior guidance, and are easily influenced by the incorrect depths or normals, especially when the truth depth scale is unavailable, while our approach only uses relative depth ratios for verifying newly generated splats, so as to relax the requirement on depth or scale accuracy.

III. SYSTEM OVERVIEW

Suppose each scene has a set of multi-view RGB images captured with digital cameras as input, denoted by $\mathcal{I} = \{I_t | t = 1, \dots, M\}$, where M is the number of input images. Our GeoTexDensifier system is applied to the multi-view images as training views to robustly reconstruct an high-quality 3DGS model of the captured scene, which we defined as \mathcal{G} . Fig. 2 outlines the proposed high-quality 3DGS framework. In the initialization stage, COLMAP [39] is carried out first to estimate camera poses of all the input views denoted as $\{\mathbf{M}_t | t = 1, \dots, M\}$, with sparse Structure-from-Motion (SfM) feature map points used to initialize a set of Gaussian splats. Meanwhile, a depth map is estimated for each input RGB image by ZoeDepth [40] with its normal map computed from depths, denoted as $\mathcal{D} = \{D_t | t = 1, \dots, M\}$ and $\mathcal{N} = \{N_t | t = 1, \dots, M\}$ respectively. After initialization finishes, the adaptive optimization stage follows to control the splat distribution by densification and pruning, while iteratively refining the Gaussian parameters to enforce their rasterized images to be consistent with the texture details observed in the training views. We use a texture-aware densification strategy to provide sufficient Gaussian splats in fully textured areas while maintaining the sparsity of Gaussians in regions with weak textures to ensure more accurate spatial distribution of Gaussian points. Additionally, the estimated depths are used as priors to guide the splitting of Gaussian splats to better

conform to the actual tangential directions of the geometric surfaces in weakly textured regions and avoid the generation of isolated or scattered Gaussians caused by the ambiguity due to lack of visual features. The texture-aware densification approach together with the geometry-guided splitting strategy constitute our geometry-texture-aware densification framework for reconstructing high-quality photorealistic 3DGS model, which will be described in detail in the following sections.

IV. PRELIMINARY

Original 3DGS [1] explicitly represents the scene with a collection of anisotropic 3D Gaussians that retains the differential properties of volumetric representation while enabling real-time rendering through a tile-based rasterization. Each Gaussian splat G_k initially derived from a sparse SfM feature point, is defined by attributes including mean position μ_k , spherical harmonic (SH) coefficients c_k to model its view-dependent color, anisotropic covariance Σ_k , and opacity α_k , with $G_k \sim \mathcal{N}(\mu_k, \Sigma_k)$. To ensure the covariance matrix Σ_k to be semi-positive definite, it is decomposed into a diagonal scaling matrix $S_k = \text{diag}([s_1 \ s_2 \ s_3]) \in \mathbb{R}^{3 \times 3}$ and a rotation quaternion $R_k = [r_1 \ r_2 \ r_3] \in \text{SO}(3)$, as $\Sigma_k = R_k S_k S_k^T R_k^T$.

3DGS renders a novel-view image n by α -blending of K depth-sorted splats for each pixel $\bar{\mathbf{x}}$ as follows:

$$\begin{aligned} C(\bar{\mathbf{x}}) &= \sum_{k=1}^K c_k w_k(\bar{\mathbf{x}}) \prod_{j=1}^{k-1} (1 - w_j(\bar{\mathbf{x}})) \\ w_k(\bar{\mathbf{x}}) &= \alpha_k \bar{G}_k(\bar{\mathbf{x}}), \end{aligned} \quad (1)$$

where $C(\bar{\mathbf{x}})$ represents the color rendered at image pixel $\bar{\mathbf{x}}$, and $w_k(\bar{\mathbf{x}})$ is the rendering weight for α -blending. $\bar{G}_k \sim \mathcal{N}(\bar{\mu}_k, \bar{\Sigma}_k)$ is the projected 2D Gaussian distribution of G_k through a local affine approximation of perspective transformation \mathbf{W} , defined as $\bar{\mu}_k = \mathbf{W}\mu_k$ and $\bar{\Sigma}_k = [\mathbf{J}\mathbf{W}\Sigma_k\mathbf{W}^T\mathbf{J}^T]_{1:2,1:2}$, with \mathbf{J} the Jacobian form of \mathbf{W} and $[\cdot]_{1:2,1:2}$ taking the first two rows and columns as sub-matrix. Finally, by leveraging the differentiable

rasterizer and comparing the rendered images to the training views, all attributes of the 3D Gaussians can be learned and optimized by minimizing the \mathcal{L}_1 loss combined with a D-SSIM loss.

During the optimization of Gaussian parameters, ADC is applied to populate Gaussian splats in the empty areas, which focuses mainly on incomplete regions with missing Gaussians defined as “under-reconstruction”, and areas covered by large-sized Gaussians as “over-reconstruction”. Gaussians with large average view-space positional gradients are to be densified, by Gaussian cloning in under-reconstructed regions and splitting large-variance splats in over-reconstructed places, to get a sufficient number of Gaussian splats for more complete reconstruction. However, even with this ADC strategy, there still might be under-densification situation in regions with full textures. Recent works such as Mini-Splatting [14], Pixel-GS [17] and Bulò et al. [29] have discussed this densification limitation and proposed corresponding densification improvement strategies to alleviate the problem. For example, Mini-Splatting incorporates blur split strategy combined with depth reinitialization to densify Gaussian splat distribution, followed by a simplification technique to suppress the total number of points for a more efficient Gaussian representation. Specifically, for each image I_t , a set of Gaussians with large blurry areas are identified by:

$$\begin{aligned} G_b^t &= \{G_i | S_i^t > \mathcal{T}\} \\ S_i^t &= \sum_{\bar{\mathbf{x}}=(1,1)}^{(W,H)} \delta(\mathbf{I}_i(\bar{\mathbf{x}}) = \mathbf{I}_{max}(\bar{\mathbf{x}})). \end{aligned} \quad (2)$$

Here S_i^t represents the maximal contribution area of Gaussian G_i to I_t , with $\mathbf{I}_i(\bar{\mathbf{x}})$ denoting the projection index of G_i at pixel $\bar{\mathbf{x}} \in I_t$ and $\mathbf{I}_{max}(\bar{\mathbf{x}}) = \arg \max_k w_k(\bar{\mathbf{x}})$ defining the rendered index with the maximal weight contribution at $\bar{\mathbf{x}}$. Threshold $\mathcal{T} = \theta WH$, with θ a coefficient on the image resolution of I_t denoted as (W, H) . The selected blurry splats are then split according to the original splitting strategy in [1] during the adaptive optimization process. Although this strategy can enrich texture details in the under-densified textured areas, it only counts the Gaussian contribution sizes without consideration of texture richness for each area, so that the textureless regions will also be split in the same way according to the blur split, which is why we propose our texture-aware strategy to take texture information into consideration for a better densification.

V. TEXTURE-AWARE DENSIFICATION

An ideal densification strategy is to maintain dense splat distribution in strongly textured areas, while still leaving Gaussian splats relatively sparse in more weakly textured regions such as surfaces with pure colors. The blur split strategy introduced by Mini-Splatting [14] is adopted in our ADC process, which is although helpful for densification, but might cause the following side effects which do not actually conform to our ideal purpose: firstly, weakly textured regions often have Gaussians with large contribution areas, leading to over-splitting of splats to consequently generate too many inadequately optimized floaters which will influence the rendering results, and the second is that an excessive number

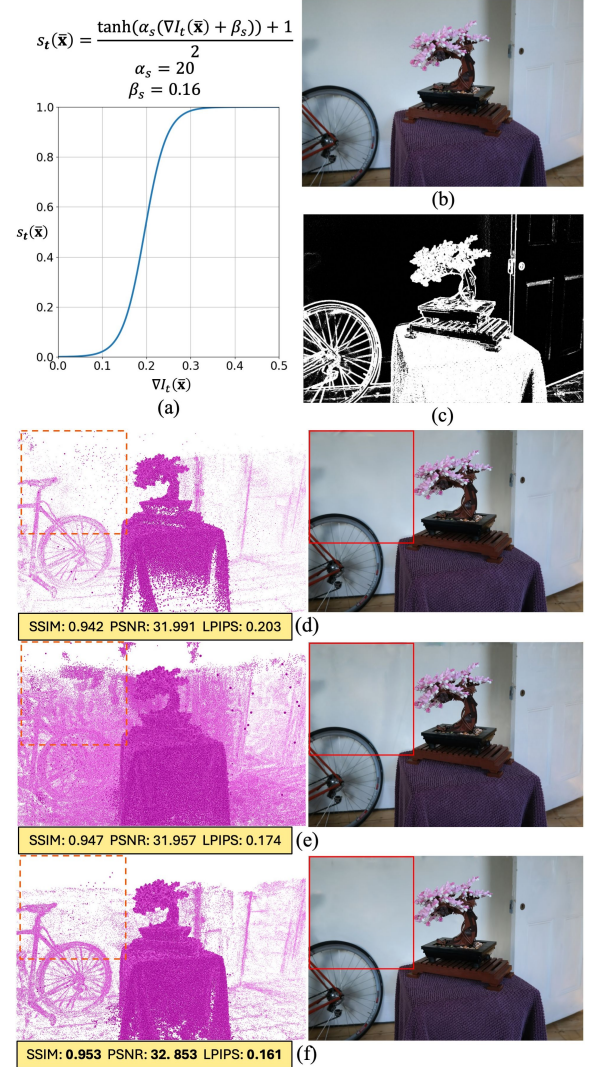


Fig. 3. An example of texture-aware densification on case “Bonsai” from Mip-NeRF 360 dataset [6]. (a) Activation function graph for $s_t(\bar{\mathbf{x}})$ by Eq. 3. (b) A representative frame with its weight map computed by $s_t(\bar{\mathbf{x}})$ given in (c). (d)-(f) are the reconstructed Gaussian point clouds and rendered images by original 3DGS [1], Mini-Splatting-D [14] and our approach, respectively, to show both the well-structured Gaussian distribution and the best rendering quality of our densification strategy according to evaluation on SSIM, PSNR and LPIPS.

of Gaussians in uniform splat distribution over the whole scene will cost too heavy memory consumption and large output file storage.

To address these issues, we propose a texture-aware densification approach, which fully leverages the texture richness of the training images to guide the densification degrees of Gaussian splats in regions of various textures, while controlling the growth of splats during the splitting process. In this way, our strategy ensures the densified splats more thoroughly optimized to improve the reconstruction quality. To better incorporate texture information as guidance, we designed a new weight $s_t(\bar{\mathbf{x}})$ for each pixel $\bar{\mathbf{x}} \in I_t$ to more reasonably count the contribution of each Gaussian G_i for identifying blur splats in Eq. 2. Activated by the texture gradient of each

training image I_t , this new weight is calculated as follows:

$$s_t(\bar{\mathbf{x}}) = \frac{\tanh(\alpha_s(\nabla I_t(\bar{\mathbf{x}}) + \beta_s)) + 1}{2}, \quad (3)$$

which effectively reflects the contribution to whether a Gaussian point should be split by a hyperbolic tangent function normalized to $[0, 1]$, which is activated by the image gradient whose gray values are normalized from $[0, 255]$ to $[0, 1]$, as shown in Fig. 3(a). α_s and β_s are the linear regression coefficients which we set to 20 and 0.16 respectively for our experiments. Fig. 3(c) shows a computed weight map by Eq. 3. With the newly defined weight, we can redefine the maximal contribution area of each Gaussian G_i to I_t as \hat{S}_i^t , by modifying Eq. 2 to:

$$\begin{aligned} G_b^t &= \{G_i | \hat{S}_i^t > \hat{\mathcal{T}}\} \\ \hat{S}_i^t &= \sum_{\bar{\mathbf{x}}=(1,1)}^{(W,H)} s_t(\bar{\mathbf{x}}) \delta(\mathbf{I}_i(\bar{\mathbf{x}}) = \mathbf{I}_{\max}(\bar{\mathbf{x}})), \end{aligned} \quad (4)$$

which collects statistics of pixel-wise texture gradients inside the contribution area of G_i on I_t instead of directly counting the contribution area S_i^t . In this way, fully textured contribution areas will have higher texture gradient statistics to consider the splats blurry and enforce them to be further split to get higher density of Gaussians, while weakly textured areas do not have sufficient texture gradient collection to support further splitting, so that their splat distributions are kept relatively sparse, as illustrated in Fig. 3(f).

The original threshold \mathcal{T} in Eq. 2 is a fixed value. For the redefined contribution area \hat{S}_i^t calculated for each Gaussian splat, we further introduce an adaptive threshold $\hat{\mathcal{T}}$ to determine whether the Gaussian point is large enough to be split, which is defined as $\hat{\mathcal{T}} = \mathcal{T}_s + (\mathcal{T}_e - \mathcal{T}_s) \frac{l - l_s}{l_e - l_s}$, where l is the current iteration number, l_s and l_e are respectively the start and end iteration numbers for densification, and \mathcal{T}_s and \mathcal{T}_e are the start and end threshold values which we set to 40 and 4 respectively for our experiments. Note that $\hat{\mathcal{T}}$ will decrease as the number of iterations increases, to give the split Gaussians with smaller contribution areas more chances to be further split and fully optimized in the next times of splitting.

Fig. 3(d)-(f) gives an ablation study on case ‘‘Bonsai’’ to verify the usefulness of our texture-aware densification strategy. From the comparison of point clouds and rendered images by original 3DGS [1], Mini-Splatting-D [14] and our approach highlighted in the rectangles, we can see that our strategy more fully densifies the strongly-textured regions compared to original 3DGS, while keeping the weakly textured regions relatively sparse compared to the over-densified Mini-Splatting, to make a compact spatial distribution of splats that also performs the best in rendering quality.

This texture-aware densification serves as an auxiliary strategy that supplements the original splitting strategy for a better ADC. Table I provides space/time resource statistics of training time, GPU peak memory (G. P. M.), and rendering frame rate (FPS) on our pipeline and Mini-Splatting-D [14], from which we can see that although our *VDRC* checking and normal guidance strategies which are described in section VI increase our training time complexity, our texture-aware splitting successfully suppresses the GPU memory usage, resulting

TABLE I
THE STATISTICS OF TIME IN MINUTES (M), GPU PEAK MEMORY (G. P. M.) CONSUMPTION (GB), AND RENDERING FRAME RATE OF THE RECONSTRUCTED 3DGS MODEL IN FRAMES PER SECOND (FPS) ON OUR PIPELINE AND MINI-SPLATTING-D [14] FOR THE CASE ‘‘BONSAI’’ FROM MIP-NERF 360 [6].

Methods	Mini-Splatting-D			Ours		
	Time	G. P. M.	FPS	Time	G. P. M.	FPS
Bonsai	28m16s	6.61GB	132	42m31s	3.75GB	177

in a smaller number of Gaussians to be rendered in a higher FPS.

VI. GEOMETRY-AWARE SPLITTING

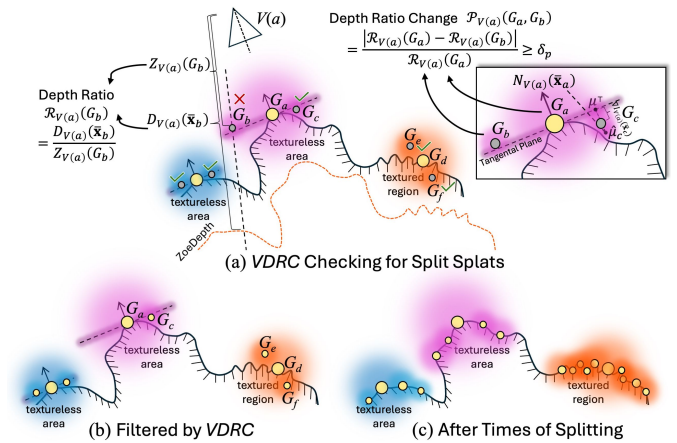


Fig. 4. A 2D simulation of our geometry-aware splitting. (a) Illustration of normal-guided splitting and *VDRC* checking for children split from their parent splats. (b) The filtered splats by *VDRC*, with noisy Gaussians eliminated and spatial distribution better fitting the actual structure. (c) The splats after several times of splitting to show the various distribution densities in textured and textureless regions.

Besides using texture information to guide the distribution of Gaussian splats to fully textured areas, the initial placement of splats is also crucial for each time of splitting. Original 3DGS approach [1] splits an existing Gaussian into new ones located randomly within the elliptical splat scale with its Probability Density Function (PDF) as sampling guidance. These split splats can be further optimized to correct places near the real geometric surface if the regions contains plenty of textures observed by sufficient training views. However, there are usually large-sized regions with weak textures or without sufficient visible training views in real world scenarios, especially indoor scenes. If the initial 3D positions of the split splats seriously deviates from the real geometric surface, it will be challenging for them to be refined to the right positions. This issue particularly occurs in textureless areas such as indoor walls, floors and doors, where the gradients of the loss function \mathcal{L}_1 is too small to move the split splats. Fig. 5(a) gives an example of this issue: a parent Gaussian G_a on a door generates a randomly split child Gaussian G_b that attempts to fit the distant wall behind. However, G_b is initially far from the wall’s real place so that its position will not be optimized significantly to the right one. More seriously,

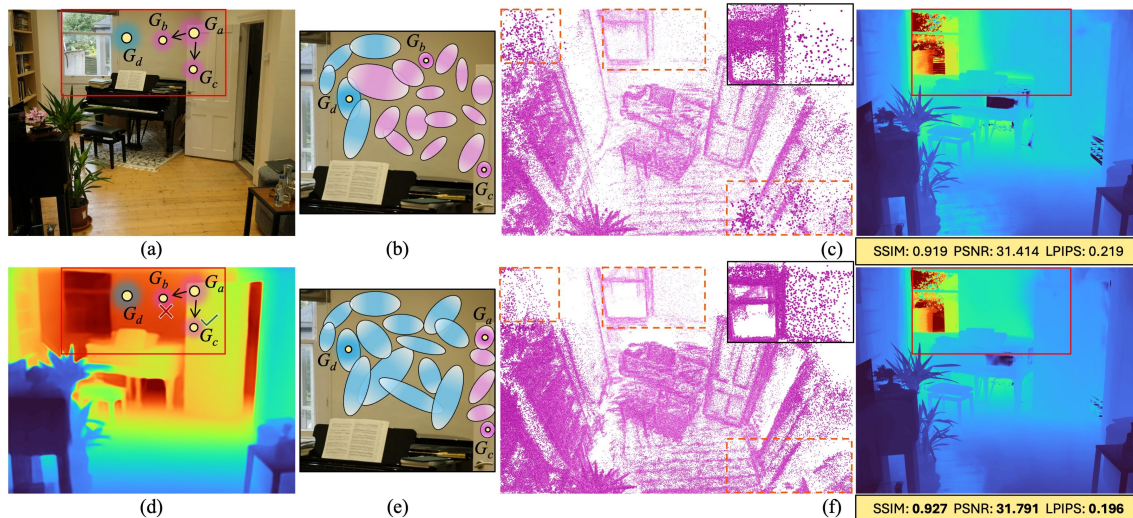


Fig. 5. VDRG for case “Room” of Mip-NeRF 360 dataset [6]. (a) A training view with two parent Gaussians denoted as G_a and G_d , where G_a attempts to be split into children G_b and G_c . (b) Original 3DGS [1] advises G_b , G_c and G_d to be continuously split into new Gaussians, resulting in scattered splats due to the improper initial placement of G_b . (c) The positions of Gaussians and the rendered depth map by original 3DGS to show noisy splats of some highlighted places like the wall. (d) The predict depth map of (a) by ZoeDepth [40]. (e) Our method discards G_b by VDRG with depth prior of (d) to make the new Gaussians split from G_a , G_c and G_d . (f) The splat positions and the rendered depth map by our method, with a more accurate geometric structure and fewer noisy points in places highlighted in red such as the wall.

G_b will continue to be split into more incorrect splats which attempt to fit the wall in the next iterations, ultimately resulting in a scattered set of noisy splats, as shown in Fig. 5(b) and (c). Conversely, another split child Gaussian G_c attempts to fit the door itself and is initially placed closer to it, which will not exhibit the same issue as G_b .

To better address this issue, we propose to leverage the depth maps of the training views estimated by ZoeDepth [40] as an additional geometric prior for validating our splitting operations, considering the robustness of ZoeDepth to complicated scenarios, especially scenes with weak textures. However, ZoeDepth predicts monocular depth maps without true scale of the captured scene. A straightforward idea is to align the depth map with the scale of sparse SfM points and check the discriminant validity of the initial placement of each newly split splat with the rescaled depth maps. Nevertheless, achieving pixel-level alignment of the monocular depth map is impractical due to the sparsity and noisy outliers of the SfM map points. Considering that the relative depths by SOTA monocular depth estimation networks like ZoeDepth are always reliable, we explore to directly utilize the relative depth information from the unscaled depth maps to achieve such discriminant checking. Consider the simulation example of Fig. 4(a), where we aim to determine that the child G_c is reasonable while the child G_b is not. We compute the projection depth of the parent G_a to its reference view $V(a)$ by $Z_{V(a)}(G_a) = [\mathbf{M}_{V(a)}\boldsymbol{\mu}_a]_z$ with $\mathbf{M}_{V(a)}$ its projection matrix, and the projection pixel $\bar{\mathbf{x}}_a = \pi(\mathbf{M}_{V(a)}\boldsymbol{\mu}_a)$, with $\pi(x, y, z) = (f_u x/z + c_u, f_v y/z + c_v)$, in which f_u and f_v are the focal lengths in uv directions of $V(a)$, and (c_u, c_v) is the optical center, with its monocular depth obtained from ZoeDepth depth map as $D_{V(a)}(\bar{\mathbf{x}}_a)$. Then, a depth ratio is obtained by $\mathcal{R}_{V(a)}(G_a) = D_{V(a)}(\bar{\mathbf{x}}_a)/Z_{V(a)}(G_a)$. Similarly, we calculate $\mathcal{R}_{V(a)}(G_b)$ and $\mathcal{R}_{V(a)}(G_c)$ respectively. After that, we compute a depth ratio change between G_a and

G_c as:

$$\mathcal{P}_{V(a)}(G_a, G_c) = \frac{|\mathcal{R}_{V(a)}(G_a) - \mathcal{R}_{V(a)}(G_c)|}{\mathcal{R}_{V(a)}(G_a)}. \quad (5)$$

It is evident that the depth ratio change between G_a and G_c is relatively small, whereas the relative depth ratio change $\mathcal{P}_{V(a)}(G_a, G_b)$ between G_a and G_b is large. We propose to discard the child splat whose relative depth ratio change from its parent splat exceeds a threshold δ_p , to prevent generating an unsuitable child Gaussian like G_b . We set $\delta_p = 0.1$ for all our experiments. If G_b is filtered out, G_a will be reserved to take its place, as shown in Fig. 4(b). We name this discriminant checking process as *Validation of Depth Ratio Change (VDRG)*. As can be seen in Fig. 5(e), thanks to the VDRG checking to filter out noisy split splats, the splats on the front door will stay inside the door instead of being split back to the wall behind. With this VDRG checking, our geometry-aware splitting is carried out whose details are given in the following subsections.

A. Reference View Selection and Updating

Intuitively, for each parent Gaussian G_a to be split, we choose the view $V(a)$ where G_a provides maximal rendering weight $w_{V(a)}(G_a)$ in α -blending as its reference view. In our implementation, two additional attributes are added to each splat: an image id $V(a)$ and its rendering weight $w_{V(a)}(G_a)$, which will be continuously updated during the training process.

Assuming that parent depth ratio $\mathcal{R}_{V(a)}(G_a)$ is reliable, we discard its child splat G_b through VDRG on condition that $\mathcal{P}_{V(a)}(G_a, G_b)$ is lower than a threshold which we set to 0.1 for all our experiments, with the child depth ratio $\mathcal{R}_{V(a)}(G_b)$ calculated also on its parent’s reference view $V(a)$ for fair comparison. As the position of G_a continues to be optimized,

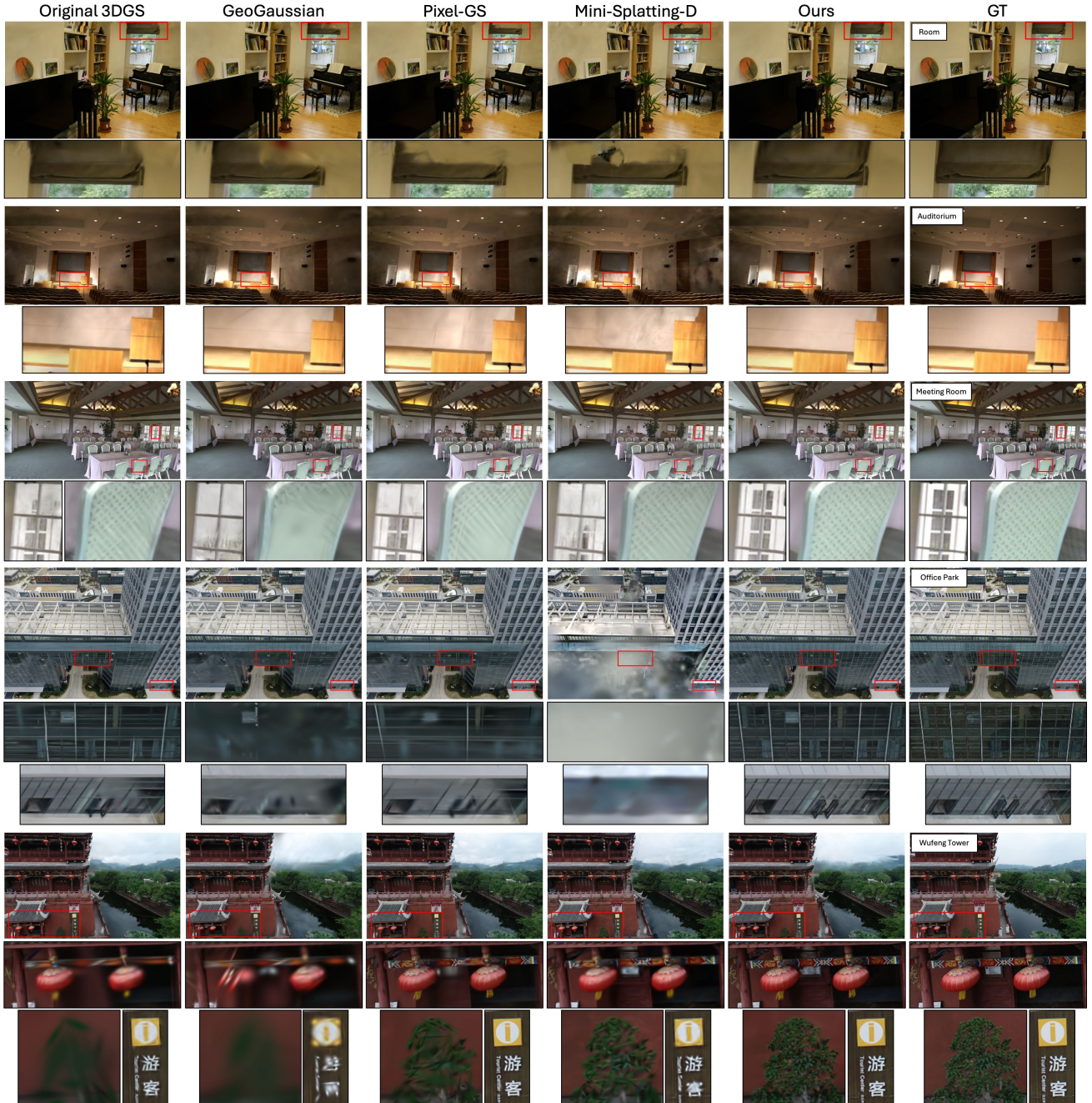


Fig. 6. Qualitative comparison of our GeoTexDensifier pipeline to original 3DGS [1], GeoGaussian [15], Pixel-GS [17] and Mini-Splatting-D [14] on the cases “Room”, “Auditorium”, “Meeting Room”, “Office Park” and “Wufeng Tower”. Some rendering details are highlighted in the rectangles to show the effectiveness of our proposed method in recovering the best texture details.

its maximal rendering weight $w_{V(a)}(G_a)$ are recalculated and compared to the recorded one. If another view provides the maximal rendering weight, $V(a)$ and $w_{V(a)}(G_a)$ will be updated iteratively.

B. VDRC for Parent Splats

Before each new time of splitting, a certain number of iterations might shift some parent splats to improper locations. For example, G_a might move from the door towards the wall, becoming an unreliable Gaussian like G_b , and will continue to generate a series of improper splats which will all meet

the condition of *VDRC*. To better solve this issue, we apply *VDRC* to the parent Gaussians before each time we split them. Since the initial Gaussians are inherited from the SfM map points, we filter out the map points whose track lengths are less than 3 or reprojection errors exceed 1 pixel, to ensure the correctness of the initial splat locations. We also choose the image view with the smallest reprojection error denoted by $\hat{V}(a)$ as the initial reference view of each Gaussian G_a , and add two additional attributes to record $\hat{V}(a)$ and its initial depth ratio $\hat{R}_{\hat{V}(a)}(G_a)$. Before each time of splitting, each optimized parent Gaussian splat G_a involved will be projected

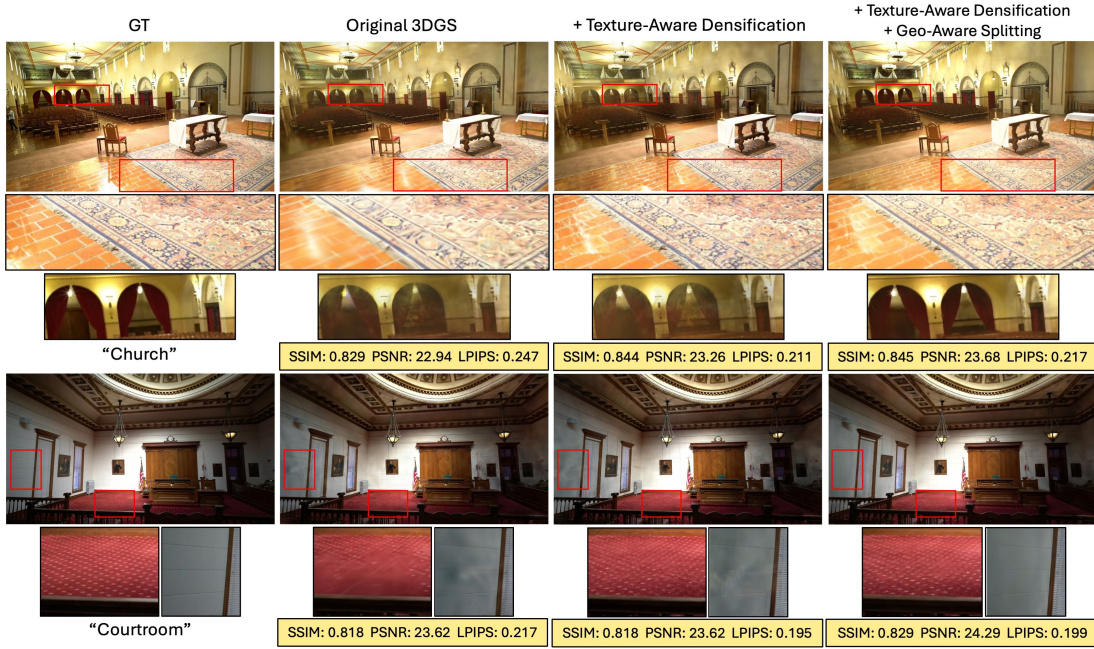


Fig. 7. Exemplar effects of our texture-aware densification and geometry-aware splitting on two cases “Church” and “Courtroom” from Tanks and Temples dataset [16]. We compare the results of original 3DGS [1], original 3DGS combined with texture-aware densification and original one with both texture-aware densification and geometry-aware splitting, with metrics evaluated to show the effectiveness of the two proposed strategies in improving rendering quality.

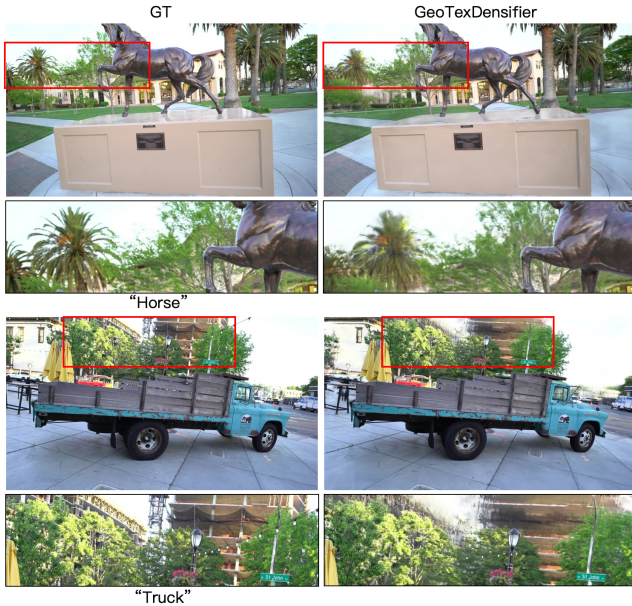


Fig. 8. Two failure cases of “Horse” and “Truck” from Tanks and Temples dataset [16]. Each case contains a representative GT testing view and the rendered 3D Gaussian splats by our GeoTexDensifier.

to its initial reference view $\hat{V}(a)$ to calculate the current depth ratio $\mathcal{R}_{\hat{V}(a)}(G_a)$, which is compared with its initial depth ratio through *VDRC* to validate its own change $\mathcal{P}_{\hat{V}(a)}(G_a) = |\hat{\mathcal{R}}_{\hat{V}(a)}(G_a) - \mathcal{R}_{\hat{V}(a)}(G_a)| / \hat{\mathcal{R}}_{\hat{V}(a)}(G_a)$. Those splats not meeting the *VDRC* requirement will be excluded from the following splitting process. If G_a is reliable by self-validation, the splitting is carried out, and *VDRC* continues to validate its two children G_b and G_c on their parent’s reference view $V(a)$



Fig. 9. VR application of rendering and navigating the “Wufeng Tower” 3DGS model reconstructed by GeoTexDensifier on Gaussian Splatting VR Viewer Unity Plugin visualized on Oculus Quest II.

by Eq. 5. The valid child splat G_c will regard its own initial reference view $\hat{V}(c)$ inherited from $V(a)$ and initial depth ratio $\hat{\mathcal{R}}_{\hat{V}(c)}(G_c) = \mathcal{R}_{V(a)}(G_c)$, which will be further used to verify whether G_c is to be divided into new Gaussians in the next time of splitting.

C. Normal Guided Splitting

Besides the use of monocular depths for checking validity of the split Gaussians, normal maps from ZoeDepth [40] are also integrated as geometric guidance for splitting into more reasonable positions. For each validated child splat G_c , original random splitting within the elliptical scale of its parent G_a will affect the smoothness and compact spatial distribution of Gaussian splats in weakly textured areas, as shown in the noisy Gaussian point cloud of Fig. 5(c). We use normal maps combined with image textures to guide the initial placement of the newly split Gaussians. Also taking the simulation of

Fig. 4(a) as example, we first project G_a and the randomly sampled G_c to the reference view $V(a)$, where the projection pixels are denoted as $\bar{\mathbf{x}}_a$ and $\bar{\mathbf{x}}_c$ respectively. Then, with the normal $N_{V(a)}(\bar{\mathbf{x}}_a)$ at $\bar{\mathbf{x}}_a$ and the image gradient $\nabla I_{V(a)}(\bar{\mathbf{x}}_c)$ at $\bar{\mathbf{x}}_c$, an optimal position of G_c can be determined as follows:

$$\begin{aligned} \mu_c &= (\hat{\mu}_c - \mu^\perp) \nabla I_{V(a)}(\bar{\mathbf{x}}_c) + \mu^\perp \\ \mu^\perp &= \hat{\mu}_c - ((\hat{\mu}_c - \mu_a) \cdot N_{V(a)}(\bar{\mathbf{x}}_a)) N_{V(a)}(\bar{\mathbf{x}}_a), \end{aligned} \quad (6)$$

where $\hat{\mu}_c$ represents the randomly sampled position of G_c , and μ^\perp is the perpendicular projection of $\hat{\mu}_c$ onto the tangential plane of G_a with $N_{V(a)}(\bar{\mathbf{x}}_a)$ as normal, whose plane equation can be represented as $(\mu_a, N_{V(a)}(\bar{\mathbf{x}}_a))$ in point-normal form, so that $N_{V(a)}(\bar{\mathbf{x}}_a) \cdot (\mu^\perp - \mu_a) = 0$. Since weakly textured regions lack sufficient visual details to enforce the split splats to move to the right positions, this normal-guided positioning enforces the child G_c to stay close to the geometric surface of the parent G_a in textureless areas with relatively small texture gradients. For fully textured areas, we believe that sufficient multi-view texture details are able to ensure the split children to be optimized to the correct places, so larger texture gradients tend to preserve the original randomness of the splat sampling instead of being excessively constrained by the geometric surface prior, as illustrated in the magnified region of Fig. 4(a).

With normal guided splitting combined with *VDRC* filtering, a better distributed Gaussian point cloud can be acquired that more accurately fits the actual scene structure with fewer noisy splats, as can be seen in the reconstructed “Room” point cloud of Fig. 5(f) which also helps to produce better rendering quality evaluated by SSIM, PSNR and LPIPS.

VII. EXPERIMENTS

We evaluate our GeoTexDensifier on nine cases from MipNeRF 360 [6], twenty one cases from Tanks and Temples [16], and two real outdoor scenes “Wufeng Tower” and “Office Park” captured by DJI Zenmuse P1 and Phantom 4 RTK respectively, each of which is composed of multi-view digital images, corresponding camera intrinsic and extrinsic parameters, and sparse SfM map points recovered by COLMAP [39]. Each experimental case typically contains some fully textured regions with appearance details, and some weakly textured surfaces. We implement GeoTexDensifier based on the source code of original 3DGS [1] and compare our implementation with original 3DGS, original 3DGS with depth prior from Depth Anything v2 (DAv2) [41], and three other SOTA methods Mini-Splatting-D [14], GeoGaussian [15] and Pixel-GS [17]. All the results are trained with the source code of each method conducted on a single Ubuntu18.04 server with an Nvidia GeForce RTX4090 GPU with 24GB memory, and 500GB RAM, with the metrics SSIM, PSNR and LPIPS given in subsection VII-A to evaluate the corresponding rendering quality. We also exhibit ablation studies on key modules such as texture-aware densification, geometry-aware splitting with *VDRC* and normal guidance in subsection VII-B to show the usefulness of each strategy on the improvements of the reconstruction quality of 3DGS models.

A. Qualitative and Quantitative Evaluation

Fig. 1 already gives an indoor scene “Church” for comparison to SOTA works. As the comparison results of other cases shown in Fig. 6 and Table II, the original 3DGS [1] often lacks sufficient splats in fully textured areas due to its simple densification strategy. Pixel-GS [17] and Mini-Splatting-D [14] address this issue to some extent, by counting the contribution of each Gaussian in two different strategies to find under-densified splats for further splitting. However, Pixel-GS still struggles to recover adequate details in the subtle textures such as the carpet in Fig. 1 and the chair in case “Meeting Room”, and seems to perform even worse in texture detail recovery than original 3DGS in self-captured case “Office Park” as shown in Fig. 6. This under-densification issue might still occur because Pixel-GS simply regards the covered pixel numbers as the weights for averaging pixel gradients, which turns out to be less adaptable to complex scenes than original strategy. On the other hand, Mini-Splatting-D employs a more explicit strategy to enforce splitting for reconstructing more texture details. Nevertheless, it suffers from over-splitting issue which further degrades reconstruction quality in areas with weak textures or insufficient training views. GeoGaussian introduces a planar regularization term to optimize the scene structure, but heavily relies on the quality of the input point cloud. Therefore, it specially uses PlanarSLAM [42] to obtain a more evenly distributed point cloud with high-quality even in weakly textured areas, which might not be suitable for general purpose. When using sparse SfM map points as input in our experiment for fair comparison, its performance is deteriorated significantly by failing to provide sufficient splats in texture-rich areas as well. Original 3DGS with depth prior is more similar to our geometry-aware splitting strategy, and outperforms the original one without depth prior. However, due to the lack of true scale for DAv2 [41], the source code implementation of original 3DGS aligns the DAv2 depth to the sparse SfM points to obtain a scale and offset for each frame as depth prior, whose accuracy might be affected by some unreliable SfM points or possible scale inconsistency across multiple frames to impact the final rendering quality. In comparison, our GeoTexDensifier fully combines texture-aware densification and geometry-aware splitting strategies to produce a 3DGS model consisting of cleaner, more reasonably and more accurately distributed splats without rely on truly scaled depth prior, which offers superior rendering quality compared to the other works as verified by the quantitative evaluation of metrics SSIM, PSNR and LPIPS given in Table II. Please refer to the supplementary material for more comparison details in the videos.

B. Ablation Studies

Fig. 1 and Fig. 3 already demonstrate that our texture-aware densification effectively recovers appearance details in texture-rich areas while maintaining sparse splat distribution in low-texture regions. Fig. 5 illustrates how our geometry-aware splitting strategy further refines the initial placement of child Gaussians, so as to help our system to achieve 3DGS models with a more reasonable spatial distribution of

TABLE II

QUANTITATIVE COMPARISON OF OUR METHOD TO ORIGINAL 3DGS [1], ORIGINAL 3DGS WITH DEPTH PRIOR [1], GEOGAUSSIAN [15], PIXEL-GS [17] AND MINI-SPLATTING-D [14] ON MIP-NeRF 360 AND TANKS AND TEMPLES DATASETS AND TWO SELF-CAPTURED OUTDOOR SCENES, WITH THE NUMBER OF GAUSSIAN SPLATS DENOTED BY $|\mathcal{G}|$ IN MILLIONS, AND EVALUATION OF RENDERING QUALITY METRICS WITH SSIM, PSNR IN DB AND LPIPS.

Methods Cases	Orig. 3DGS				Orig. 3DGS + Depth Prior				GeoGaussian				Pixel-GS				Mini-Splating-D				Ours			
	$ \mathcal{G} $	SSIM	PSNR	LPIPS	$ \mathcal{G} $	SSIM	PSNR	LPIPS	$ \mathcal{G} $	SSIM	PSNR	LPIPS	$ \mathcal{G} $	SSIM	PSNR	LPIPS	$ \mathcal{G} $	SSIM	PSNR	LPIPS	$ \mathcal{G} $	SSIM	PSNR	LPIPS
Bicycle (Mip-NeRF 360)	6.1	0.765	25.205	0.21	5.24	0.763	25.216	0.215	2.8	0.75	24.891	0.237	9.06	0.778	25.265	0.181	6.02	0.798	25.542	0.158	6.03	0.782	25.388	0.177
Garden	5.88	0.866	27.34	0.107	4.12	0.864	27.39	0.109	2.91	0.858	27.117	0.121	8.78	0.871	27.492	0.098	5.82	0.877	27.517	0.091	5.36	0.87	27.561	0.104
Stump	4.92	0.773	26.621	0.215	4.42	0.77	26.593	0.217	1.93	0.753	25.502	0.247	6.66	0.786	26.842	0.187	5.37	0.804	27.114	0.169	4.93	0.786	26.874	0.195
Treehill	3.77	0.633	22.523	0.325	3.37	0.634	22.525	0.325	1.91	0.629	22.058	0.344	7.97	0.634	22.21	0.276	4.86	0.641	22.222	0.261	3.73	0.635	22.379	0.293
Flowers	3.63	0.606	21.578	0.336	3.22	0.606	21.582	0.338	2.09	0.578	21.065	0.371	7.48	0.635	21.546	0.262	4.87	0.643	21.528	0.254	6.18	0.621	21.251	0.26
Room	1.54	0.919	31.414	0.219	1.37	0.919	30.982	0.218	0.62	0.901	29.908	0.251	2.57	0.922	31.579	0.208	3.93	0.928	31.576	0.187	2.55	0.927	31.93	0.195
Counter	1.21	0.909	28.993	0.2	1.13	0.907	28.874	0.2	0.56	0.889	27.899	0.235	2.57	0.915	29.186	0.183	3.78	0.913	28.728	0.171	1.74	0.916	29.216	0.179
Bonsai	1.26	0.942	31.991	0.203	1.15	0.94	32.219	0.204	0.76	0.925	31.026	0.225	2.08	0.947	32.554	0.191	3.76	0.947	31.957	0.174	1.83	0.954	32.952	0.161
Kitchen	1.82	0.926	31.036	0.127	1.6	0.924	30.999	0.128	0.73	0.908	29.207	0.148	3.19	0.931	31.702	0.119	3.67	0.933	31.802	0.114	2.09	0.931	31.698	0.12
Courtroom (Tanks & Temples)	2.99	0.818	23.621	0.217	3.23	0.806	23.788	0.218	1.47	0.797	23.152	0.265	5.18	0.818	23.719	0.215	5.24	0.792	21.73	0.219	4.78	0.829	24.287	0.199
Auditorium	0.69	0.881	24.083	0.247	0.77	0.871	24.793	0.264	0.25	0.867	23.765	0.292	1.21	0.883	24.351	0.244	4.8	0.839	21.506	0.274	1.64	0.892	25.24	0.234
Meetingroom	1.33	0.88	25.664	0.216	1.39	0.865	25.699	0.227	0.57	0.861	24.752	0.264	3.16	0.881	25.857	0.21	4.21	0.869	24.859	0.21	2.2	0.888	26.355	0.204
Church	2.24	0.829	22.946	0.247	2.61	0.804	22.553	0.266	1	0.811	22.355	0.279	3.61	0.833	23.317	0.243	4.86	0.818	21.89	0.241	4.08	0.845	23.678	0.217
Ballroom	3.42	0.807	23.902	0.188	3.33	0.813	24.236	0.183	1.23	0.788	23.31	0.141	6.07	0.808	23.843	0.181	4.61	0.806	23.49	0.179	4.45	0.815	23.99	0.17
Museum	5.34	0.774	21.22	0.235	4.49	0.788	21.956	0.222	2.42	0.76	20.43	0.176	9.62	0.769	21.15	0.239	6.09	0.77	20.624	0.231	4.76	0.778	21.527	0.226
Barn	1.03	0.817	26.828	0.259	1.13	0.815	26.921	0.256	0.39	0.788	25.54	0.24	4.22	0.84	27.234	0.215	3.88	0.862	27.455	0.175	4.02	0.856	27.472	0.128
Caterpillar	1.22	0.733	22.738	0.3	1.52	0.74	22.608	0.292	0.42	0.692	21.45	0.297	3.96	0.773	23.051	0.243	3.9	0.773	22.667	0.232	3.07	0.775	23.185	0.28
Courthouse	0.62	0.781	21.919	0.288	0.89	0.79	22.305	0.271	0.2	0.755	20.57	0.306	1.36	0.787	22.126	0.279	5.75	0.736	19.073	0.326	1.23	0.796	22.194	0.254
Family	2.31	0.844	24.024	0.191	2.23	0.848	24.289	0.182	1.12	0.807	22.460	0.164	3.86	0.847	23.942	0.174	4.21	0.856	24.27	0.154	2.07	0.848	24.218	0.187
Francis	0.81	0.881	27.188	0.265	0.87	0.883	27.798	0.267	0.36	0.86	25.13	0.162	2.02	0.889	27.521	0.249	3.89	0.888	26.203	0.238	1.27	0.888	27.375	0.245
Horse	1.32	0.866	23.481	0.187	1.49	0.874	24.249	0.175	0.72	0.85	22.73	0.139	2.39	0.869	23.744	0.167	3.91	0.87	23.849	0.152	1.18	0.862	23.613	0.187
Ignatius	3.45	0.732	21.245	0.264	2.96	0.736	21.817	0.259	1.56	0.704	20.460	0.234	5.92	0.744	21.59	0.235	4.75	0.747	21.273	0.217	4.46	0.744	21.781	0.228
Lighthouse	0.85	0.826	21.966	0.234	0.97	0.83	22.612	0.224	0.26	0.803	21.08	0.192	2.81	0.825	21.495	0.225	4.76	0.79	18.679	0.225	0.88	0.83	22.434	0.218
M60	1.75	0.887	26.839	0.195	1.58	0.889	27.361	0.193	0.75	0.87	26.040	0.151	5.04	0.896	27.329	0.164	4.14	0.895	26.961	0.153	2.42	0.895	27.17	0.163
Palace	0.66	0.741	19.936	0.359	0.84	0.745	20.398	0.342	0.23	0.725	19.51	0.358	1.90	0.746	20.014	0.346	7.28	0.666	15.467	0.444	0.85	0.751	20.352	0.326
Panther	1.96	0.894	27.734	0.185	1.73	0.894	27.753	0.185	0.96	0.882	27.04	0.122	5.14	0.899	27.705	0.158	4.41	0.871	25.571	0.184	1.79	0.896	27.675	0.177
Playground	2.32	0.801	24.209	0.267	2.03	0.805	24.684	0.262	1.15	0.775	23.3	0.224	4.17	0.832	24.829	0.217	4.56	0.871	25.571	0.184	3.21	0.835	24.853	0.197
Temple	0.76	0.788	20.021	0.292	1.03	0.804	21.072	0.27	0.29	0.772	19.630	0.27	3.38	0.789	19.993	0.272	5.46	0.7	15.755	0.358	0.91	0.795	20.483	0.266
Train	0.93	0.762	21.269	0.282	1.28	0.771	21.438	0.265	0.32	0.728	20.05	0.27	3.5	0.778	21.076	0.25	4.05	0.766	19.621	0.25	2.59	0.785	21.264	0.224
Truck	2.88	0.816	23.157	0.236	2.64	0.819	23.5	0.227	1.2	0.791	22.18	0.155	6.23	0.823	23.314	0.204	4.64	0.83	23.263	0.165	2.74	0.819	23.199	0.226
Wufeng Tower	4.69	0.775	23.073	0.292	5.21	0.781	23.151	0.286	1.62	0.729	21.351	0.355	11.98	0.777	22.848	0.267	5.86	0.768	22.495	0.273	10.34	0.8	23.402	0.232
Office Park	2.09	0.684	22.96	0.42	2.37	0.819	23.394	0.396	0.53	0.643	22.588	0.477	1.82	0.668	22.991	0.448	7.16	0.527	15.413	0.557	7.02	0.754	24.309	0.327

TABLE III

ABLATION COMPARISONS OF ONLY GEOMETRY-AWARE SPLITTING (Geo.), ONLY TEXTURE-AWARE DENSIFICATION (Tex.), TEXTURE-AWARE DENSIFICATION WITH VDRC (DEPTH PRIOR) (Tex. + VDRC), TEXTURE-AWARE DENSIFICATION WITH NORMAL GUIDANCE (Tex. + Normal), AND GEOTEXDENSIFIER (Tex. + Geo.) ON MIP-NeRF 360 [6], WITH THE NUMBER OF GAUSSIAN SPLATS DENOTED BY $|\mathcal{G}|$ IN MILLIONS, AND EVALUATION OF RENDERING QUALITY METRICS WITH SSIM, PSNR IN DB AND LPIPS.

Methods Cases	Only Geo. (VDRC + Normal)				Only Tex.				Tex. + VDRC				Tex. + Normal				GeoTexDensifier (Tex. + Geo.)			
	$ \mathcal{G} $	SSIM	PSNR	LPIPS	$ \mathcal{G} $	SSIM	PSNR	LPIPS	$ \mathcal{G} $	SSIM	PSNR	LPIPS	$ \mathcal{G} $	SSIM	PSNR	LPIPS	$ \mathcal{G} $	SSIM	PSNR	LPIPS
Bicycle	5.49	0.771	25.262	0.199	6.28	0.777	25.372	0.19	5.73	0.78	25.367	0.186	5.81	0.78	25.407	0.187	6.03	0.782	25.388	0.177
Garden	5.33	0.868	27.433	0.105	5.91	0.869	27.536	0.105	5.36	0.87	27.541	0.103	5.37	0.87	27.555	0.103	5.36	0.87	27.561	0.104
Stump	4.82	0.776	26.672	0.209	4.97	0.783	26.775	0.196	5.02	0.786	26.866	0.195	4.67	0.786	26.869	0.196	4.93	0.786	26.874	0.195
Treehill	3.43	0.663	22.367	0.324	4.14	0.631	22.282	0.29	3.63	0.633	22.315	0.293	3.8	0.635	22.422	0.292	3.73	0.635	22.379	0.293
Flower	3.51	0.607	21.478	0.334	7.74	0.613	21.132	0.261	6.29	0.621	21.23	0.259	6.38	0.621	21.21	0.258	6.18	0.621	21.251	0.26
Room	1.43	0.919	31.455	0.218	3.82	0.926	31.493	0.193	2.52	0.927	31.713	0.196	2.67	0.927	31.755	0.194	2.55	0.927	31.93	0.195
Counter	1.06	0.907	28.88	0.201	2.29	0.915	29.183	0.177	1.7	0.915	29.178	0.18	1.74	0.915	29.191	0.18	1.74	0.916	29.216	0.179
Bonsai	1.1	0.948	32.477	0.207	2.15	0.954	32.947	0.158	1.81	0.954	32.674	0.161	1.84	0.954	32.95	0.161	1.83	0.954	32.952	0.161
Kitchen	1.39	0.926	31.138	0.127	2.68	0.931	31.641	0.118	2.12	0.931	31.463	0.119	2.1	0.931	31.331	0.119	2.09	0.931	31.698	0.12

splats. From more visualized comparisons and corresponding evaluation metrics presented in Fig. 7 we can see that, without the geometry-aware splitting strategy, the system might still encounter issues such as floater noise due to unrestricted splat placement in low-texture areas or the regions with insufficient training views, while our GeoTexDensifier with both strategies achieves the best in both fully and weakly textured regions.

Table III further provides more quantitative comparisons of ablation strategies including only geometry-aware splitting (Geo.),

via *VDRC* checking. However, this strategy might introduce a limitation in object-centric scenarios captured with distant backgrounds such as the two outdoor cases of “Horse” and “Truck” from Tanks and Temples dataset [16] shown in Fig. 8. Initial SfM points for such distant regions are usually sparse or missing. When Gaussian splats in foreground regions undergo splitting, the large relative depth ratio changes on foreground/background boundary regions typically fail to pass the *VDRC* checking, which consequently prevent these splats to be split to the distant regions, leading to “under-reconstruction” regions with missing Gaussians. These incomplete regions possibly cause blurs or ghosting artifacts in the distant backgrounds from certain viewpoints, as exemplified in the magnified regions of the representative views of the two cases in Fig. 8.

D. VR Application

We can also import the 3DGS model generated by our GeoTexDensifier into an open-sourced “Gaussian Splatting VR Viewer Unity Native Plugin”¹ to achieve photorealistic immersive visualization and real-time interactive navigation of the reconstructed scene on an Oculus Quest II standalone VR headset equipped with a single Ubuntu18.04 desktop PC with Intel Core i7-8700 CPU @ 3.2GHz, an Nvidia GeForce RTX4090 GPU, and 48GB RAM, as illustrated in Fig. 9. Note that the example of the “Wufeng Tower” can be immersively navigated by 3DGS representation with highly restored geometry and texture details. Please refer to the supplementary video for the complete demo.

VIII. CONCLUSION AND FUTURE WORK

We introduce GeoTexDensifier, a novel framework designed to more effectively enhance the densification of 3DGS, which begins with a texture-aware densification strategy that leverages texture gradients from training images to ensure the splats to be adequately populated in highly-textured areas while maintaining sparsity in regions with low textures, followed by employing a geometry-aware splitting module to guide the spatial distribution of splats to be better aligned with the actual surface of the scene by validating the initially split splat positions according to the relative depth priors. As a result, a high-quality 3DGS model is produced with more reasonably distributed splats and less noise compared to SOTA methods, leading to more photorealistic NVS effects.

Our limitation in object-centric scenes with distant backgrounds discussed in section VII-C can be better solved by combining a more reliable dense point cloud initialization instead of sparse SfM points to further avoid “under-reconstruction” situation. Besides, like other SOTA methods, our approach introduces more splats to reconstruct finer details in textured areas, which results in higher GPU memory consumption than original 3DGS when handling large-scale scenes. Our *VDRC* checking and normal guidance operations also increase the training time complexity. We plan to extend our method to support urban-scale reconstruction and

navigation in a more space/time-efficient way by integrating techniques such as chunk-based reconstruction, LOD organization and dynamically scheduled rendering. Additionally, the potential possibility of combining our approach with generative diffusion models will be explored as a future work to further enhance reconstruction completion and quality in insufficiently observed or invisible regions.

ACKNOWLEDGMENTS

The authors wish to thank Zhuang Zhang, Chongshan Sheng, Fei Jiao, Xia Sun, Jinyi Liao, Renzhi Wang, Yuqing Xie, Bingze Li and Hongliang Sun for their kind helps in the development and the experiments of the proposed GeoTexDensifier system. This work was partially supported by Key R&D Program of Zhejiang Province (No. 2023C01039), and NSF of China (No. 62425209).

REFERENCES

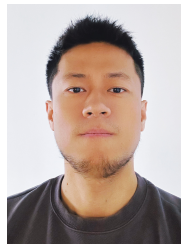
- [1] B. Kerbl, G. Kopanas, T. Leimkühler, and G. Drettakis, “3D Gaussian splatting for real-time radiance field rendering,” *ACM Transactions on Graphics*, vol. 42, no. 4, pp. 139–1, 2023.
- [2] S. M. Seitz, B. Curless, J. Diebel, D. Scharstein, and R. Szeliski, “A comparison and evaluation of multi-view stereo reconstruction algorithms,” in *IEEE Conference on Computer Vision and Pattern Recognition*, vol. 1. IEEE, 2006, pp. 519–528.
- [3] J. L. Schönberger, E. Zheng, M. Pollefeys, and J.-M. Frahm, “Pixel-wise view selection for unstructured multi-view stereo,” in *European Conference on Computer Vision*. Springer, 2016, pp. 501–518.
- [4] S. Fuhrmann, F. Langguth, and M. Goesele, “MVE—a multi-view reconstruction environment,” *GCH*, vol. 3, p. 4, 2014.
- [5] B. Mildenhall, P. P. Srinivasan, M. Tancik, J. T. Barron, R. Ramamoorthi, and R. Ng, “NeRF: Representing scenes as neural radiance fields for view synthesis,” *Communications of the ACM*, vol. 65, no. 1, pp. 99–106, 2021.
- [6] J. T. Barron, B. Mildenhall, D. Verbin, P. P. Srinivasan, and P. Hedman, “Mip-NeRF 360: Unbounded anti-aliased neural radiance fields,” in *IEEE/CVF Conference on Computer Vision and Pattern Recognition*, 2022, pp. 5470–5479.
- [7] —, “Zip-NeRF: Anti-aliased grid-based neural radiance fields,” in *IEEE/CVF International Conference on Computer Vision*, 2023, pp. 19 697–19 705.
- [8] A. Guédon and V. Lepetit, “SuGaR: Surface-aligned Gaussian splatting for efficient 3D mesh reconstruction and high-quality mesh rendering,” in *IEEE/CVF Conference on Computer Vision and Pattern Recognition*, 2024, pp. 5354–5363.
- [9] J. Waczyńska, P. Borycki, S. Tadeja, J. Tabor, and P. Spurek, “GaMeS: Mesh-based adapting and modification of Gaussian splatting,” *arXiv preprint arXiv:2402.01459*, 2024.
- [10] X. Gao, X. Li, Y. Zhuang, Q. Zhang, W. Hu, C. Zhang, Y. Yao, Y. Shan, and L. Quan, “Mani-GS: Gaussian splatting manipulation with triangular mesh,” *arXiv preprint arXiv:2405.17811*, 2024.
- [11] J. Wang, J. Fang, X. Zhang, L. Xie, and Q. Tian, “GaussianEditor: Editing 3D Gaussians delicately with text instructions,” in *IEEE/CVF Conference on Computer Vision and Pattern Recognition*, 2024, pp. 20 902–20 911.
- [12] J. Gao, C. Gu, Y. Lin, H. Zhu, X. Cao, L. Zhang, and Y. Yao, “Relightable 3D Gaussian: Real-time point cloud relighting with BRDF decomposition and ray tracing,” *arXiv preprint arXiv:2311.16043*, 2023.
- [13] T. Xie, Z. Zong, Y. Qiu, X. Li, Y. Feng, Y. Yang, and C. Jiang, “Phys-Gaussian: Physics-integrated 3D Gaussians for generative dynamics,” in *IEEE/CVF Conference on Computer Vision and Pattern Recognition*, 2024, pp. 4389–4398.
- [14] G. Fang and B. Wang, “Mini-Splatting: Representing scenes with a constrained number of Gaussians,” *arXiv preprint arXiv:2403.14166*, 2024.
- [15] Y. Li, C. Lyu, Y. Di, G. Zhai, G. H. Lee, and F. Tombari, “GeoGaussian: Geometry-aware Gaussian splatting for scene rendering,” *arXiv preprint arXiv:2403.11324*, 2024.

¹<https://github.com/clarte53/GaussianSplattingVRViewerUnity>

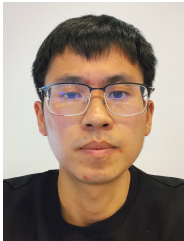
- [16] A. Knapitsch, J. Park, Q.-Y. Zhou, and V. Koltun, "Tanks and Temples: Benchmarking large-scale scene reconstruction," *ACM Transactions on Graphics*, vol. 36, no. 4, pp. 1–13, 2017.
- [17] Z. Zhang, W. Hu, Y. Lao, T. He, and H. Zhao, "Pixel-GS: Density control with pixel-aware gradient for 3D Gaussian splatting," *arXiv preprint arXiv:2403.15530*, 2024.
- [18] J. T. Barron, B. Mildenhall, M. Tancik, P. Hedman, R. Martin-Brualla, and P. P. Srinivasan, "Mip-NeRF: A multiscale representation for anti-aliasing neural radiance fields," in *IEEE/CVF International Conference on Computer Vision*, 2021, pp. 5855–5864.
- [19] T. Müller, A. Evans, C. Schied, and A. Keller, "Instant neural graphics primitives with a multiresolution hash encoding," *ACM Transactions on Graphics*, vol. 41, no. 4, pp. 1–15, 2022.
- [20] C. Sun, M. Sun, and H.-T. Chen, "Direct voxel grid optimization: Super-fast convergence for radiance fields reconstruction," in *IEEE/CVF Conference on Computer Vision and Pattern Recognition*, 2022, pp. 5459–5469.
- [21] Q. Xu, Z. Xu, J. Philip, S. Bi, Z. Shu, K. Sunkavalli, and U. Neumann, "Point-NeRF: Point-based neural radiance fields," in *IEEE/CVF Conference on Computer Vision and Pattern Recognition*, 2022, pp. 5438–5448.
- [22] Z. Chen, Z. Li, L. Song, L. Chen, J. Yu, J. Yuan, and Y. Xu, "NeuRBF: A neural fields representation with adaptive radial basis functions," in *IEEE/CVF International Conference on Computer Vision*, 2023, pp. 4182–4194.
- [23] J. Kulhanek and T. Sattler, "Tetra-NeRF: Representing neural radiance fields using tetrahedra," in *IEEE/CVF International Conference on Computer Vision*, 2023, pp. 18 458–18 469.
- [24] J. Lin, Z. Li, X. Tang, J. Liu, S. Liu, J. Liu, Y. Lu, X. Wu, S. Xu, Y. Yan *et al.*, "VastGaussian: Vast 3D Gaussians for large scene reconstruction," in *IEEE/CVF Conference on Computer Vision and Pattern Recognition*, 2024, pp. 5166–5175.
- [25] Y. Liu, H. Guan, C. Luo, L. Fan, J. Peng, and Z. Zhang, "CityGaussian: Real-time high-quality large-scale scene rendering with Gaussians," *arXiv preprint arXiv:2404.01133*, 2024.
- [26] Z. Yan, W. F. Low, Y. Chen, and G. H. Lee, "Multi-scale 3D Gaussian splatting for anti-aliased rendering," in *IEEE/CVF Conference on Computer Vision and Pattern Recognition*, 2024, pp. 20 923–20 931.
- [27] Y. Jiang, J. Tu, Y. Liu, X. Gao, X. Long, W. Wang, and Y. Ma, "GaussianShader: 3D Gaussian splatting with shading functions for reflective surfaces," in *IEEE/CVF Conference on Computer Vision and Pattern Recognition*, 2024, pp. 5322–5332.
- [28] Z. Yu, A. Chen, B. Huang, T. Sattler, and A. Geiger, "Mip-Splatting: Alias-free 3D Gaussian splatting," in *IEEE/CVF Conference on Computer Vision and Pattern Recognition*, 2024, pp. 19 447–19 456.
- [29] S. R. Bulò, L. Porzi, and P. Kotschieder, "Revising densification in Gaussian splatting," *arXiv preprint arXiv:2404.06109*, 2024.
- [30] J. Zhang, F. Zhan, M. Xu, S. Lu, and E. Xing, "FreGS: 3D Gaussian splatting with progressive frequency regularization," in *Proceedings of the IEEE/CVF Conference on Computer Vision and Pattern Recognition*, 2024, pp. 21 424–21 433.
- [31] Z. Zhu, Z. Fan, Y. Jiang, and Z. Wang, "FSGS: Real-time few-shot view synthesis using Gaussian splatting," *arXiv preprint arXiv:2312.00451*, 2023.
- [32] T. Lu, M. Yu, L. Xu, Y. Xiangli, L. Wang, D. Lin, and B. Dai, "Scaffold-GS: Structured 3D Gaussians for view-adaptive rendering," in *IEEE/CVF Conference on Computer Vision and Pattern Recognition*, 2024, pp. 20 654–20 664.
- [33] Z. Yu, S. Peng, M. Niemeyer, T. Sattler, and A. Geiger, "MonoSDF: Exploring monocular geometric cues for neural implicit surface reconstruction," *Advances in Neural Information Processing Systems*, vol. 35, pp. 25 018–25 032, 2022.
- [34] M. Turkulainen, X. Ren, I. Melekhov, O. Seiskari, E. Rahtu, and J. Kannala, "DN-Splatter: Depth and normal priors for Gaussian splatting and meshing," *arXiv preprint arXiv:2403.17822*, 2024.
- [35] J. Li, J. Zhang, X. Bai, J. Zheng, X. Ning, J. Zhou, and L. Gu, "DNGaussian: Optimizing sparse-view 3D Gaussian radiance fields with global-local depth normalization," in *IEEE/CVF Conference on Computer Vision and Pattern Recognition*, 2024, pp. 20 775–20 785.
- [36] D. Chen, H. Li, W. Ye, Y. Wang, W. Xie, S. Zhai, N. Wang, H. Liu, H. Bao, and G. Zhang, "PGSR: Planar-based Gaussian splatting for efficient and high-fidelity surface reconstruction," *arXiv preprint arXiv:2406.06521*, 2024.
- [37] H. Xiang, X. Li, X. Lai, W. Zhang, Z. Liao, K. Cheng, and X. Liu, "GaussianRoom: Improving 3D Gaussian splatting with SDF guidance and monocular cues for indoor scene reconstruction," *arXiv preprint arXiv:2405.19671*, 2024.
- [38] M. Yu, T. Lu, L. Xu, L. Jiang, Y. Xiangli, and B. Dai, "GSDF: 3DGS meets SDF for improved rendering and reconstruction," *arXiv preprint arXiv:2403.16964*, 2024.
- [39] J. L. Schönberger and J.-M. Frahm, "Structure-from-motion revisited," in *IEEE Conference on Computer Vision and Pattern Recognition*, 2016, pp. 4104–4113.
- [40] S. F. Bhat, R. Birkel, D. Wofk, P. Wonka, and M. Müller, "ZoeDepth: Zero-shot transfer by combining relative and metric depth," *arXiv preprint arXiv:2302.12288*, 2023.
- [41] L. Yang, B. Kang, Z. Huang, Z. Zhao, X. Xu, J. Feng, and H. Zhao, "Depth Anything V2," *Advances in Neural Information Processing Systems*, vol. 37, pp. 21 875–21 911, 2024.
- [42] Y. Li, R. Yunus, N. Brasch, N. Navab, and F. Tombari, "RGB-D SLAM with structural regularities," in *IEEE International Conference on Robotics and Automation*. IEEE, 2021, pp. 11 581–11 587.



Hanqing Jiang received his Ph.D. degree from Zhejiang University, after which he was a postdoctoral researcher in the State Key Lab of CAD&CG, Zhejiang University. He is currently a Research Director in SenseTime Group Ltd, China. He received the best paper award of ISMAR 2020 and the best journal paper nominee of ISMAR 2021. His research interests focus on computer vision, including video enhancement, multi-view stereo, 3D reconstruction, neural radiance fields, and augmented reality.



Xiaoyu Zhang is a researcher at SenseTime Group Ltd, China. He received his master's degree from Northwestern Polytechnical University in 2019. His research interests include novel view synthesis and 3D reconstruction.



Xiaojun Xiang received his master degree from the State Key Lab of CAD&CG, Zhejiang University. He is currently a Senior Researcher in SenseTime Group Ltd, China. He received the best journal paper nominee of ISMAR 2021. His research interests lie in the field of 3D computer vision, including multi-view stereo, vectorized modeling, and implicit neural reconstruction.



Guofeng Zhang is now a professor at State Key Lab of CAD&CG, Zhejiang University. He received his BS and Ph.D. degrees in Computer Science from Zhejiang University, in 2003 and 2009, respectively. He received the National Excellent Doctoral Dissertation Award, the Excellent Doctoral Dissertation Award of China Computer Federation and the best paper award of ISMAR 2020. His research interests include structure-from-motion, SLAM, 3D reconstruction, augmented reality, spatial intelligence.



Han Sun is currently a researcher in SenseTime Group Ltd, China. He received his master degree from University of Science and Technology of China in 2018. His research interests include structure from motion, multi-view stereo, and 3D reconstruction.



Hongjie Li received the M.S. and Ph.D degrees in photogrammetry and remote sensing from the State Key Laboratory of Information Engineering in Surveying, Mapping and Remote Sensing (LIES-MARS), Wuhan University, Wuhan, China, in 2020 and 2024, respectively. He is currently a Researcher in SenseTime Group Ltd, China. His research interests include multi-view stereo, 3D reconstruction and 3D generation.



Liyang Zhou is currently a Senior Algorithm Engineer in SenseTime Group Ltd, China. He received his master degree from Zhejiang University in 2016, and the best paper award of ISMAR 2020. His research interests include structure from motion, multi-view stereo, and 3D reconstruction.